physica status solidi pss rrl
www.pss-rapid.com

Near-Infrared Organic Phototransistors Based on Thermally Evaporated Planar Heterojunctions

Liye Yang, Shuai Sun, Liangyu Zhang, Muhammad Irfan, Mengpei Zhang, Paul K. Chu, Yang Jiao, and Jia Li**

Heterostructures are widely used in organic phototransistors (OPTs) to balance carrier dynamics, including exciton dissociation, transport, and recombination inhibition. Planar heterojunctions (PHJs) offer direct pathways and fewer recombination sites for photo-induced carriers. However, PHJ-based OPTs' performance remains unsatisfactory due to challenges in achieving high-quality organic planar interfaces with uniformity, large area, low roughness, and low defect density. Herein, a PHJ structure is designed for near-infrared (NIR) photodetection. The PHJ consists of a polymer semiconductor, PDPPBTT, and a fullerene derivative, $PC_{61}BM$. The PDPPBTT acts as the NIR photoactive layer, electron donor, and channel, while $PC_{61}BM$ is the acceptor. A simple evaporation technique is developed to deposit the $PC_{61}BM$ film on PDPPBTT to form a stable and uniform planar interface. Owing to the balanced dynamic characteristics, highly sensitive NIR photodetection is achieved as demonstrated by peak photosensitivity of 2.59×10^4, photoresponsivity of 1.42×10^5 A W^{-1}, detectivity of 1.83×10^{16} Jones upon weak irradiation of 0.072 μW cm^{-2}. To confirm the practicality of NIR imaging, a 7×7 array device is demonstrated. The results reveal a simple and effective strategy to prepare high-performance PHJ-based OPTs and provide insights into the development of advanced photodetection and imaging systems.

1. Introduction

Advanced near-infrared (NIR) photodetectors have immense potential for applications in lidar, health monitoring, and quantum technologies.[1–6] Organic phototransistors (OPTs) have recently attracted a lot of attention because the channel carrier density can be modulated by both electrical gating and incident photons to combine the gains from both the transistor and photoconductor.[7–10] Owing to the intrinsic high-gain effect, signal amplification can be accomplished without noise increase to produce high photosensitivity and low detection limits.[11–13]

Heterostructures are extensively used in OPTs and play important roles in exciton dissociation, photon absorption, exciton dissociation, and recombination inhibition. In this respect, many heterostructures have been designed by combining the appropriate donor and acceptor materials.[4,13,14] Most of the reported NIR-OPTs adopt a device architecture consisting of a bulk heterojunction (BHJ) formed by mixing the electron donor (D) and acceptor (A) in the photoactive thin film.[13,15–17] The bi-continuous 3D interpenetrating network of BHJ provides the maximum discrete D/A interface area to facilitate exciton dissociation due to short exciton diffusion length and improve the properties of OPTs. However, despite recent developments, BHJ-OPTs still face many challenges. First of all, precise tailoring of the degree of D/A phase separation is vital to the optimal pathway for charge transport while maintaining a large interfacial area for exciton dissociation, but it is difficult. Secondly, the random distribution of D/A materials in the BHJ results in tortuous pathways for charge carriers. This increases the distance charge carriers must travel as well as the probability of encountering recombination sites, thereby decreasing the overall carrier mobility of OPTs.[12,16,18–20]

Alternatively, a planar heterojunction (PHJ) is a possibility for OPTs.[20–22] In comparison with BHJ, PHJ has an ordered

L. Yang, Y. Jiao
School of Physics
Northwest University
Xi 'an 710127, China
E-mail: yjiao@nwu.edu.cn

L. Yang, S. Sun, L. Zhang, M. Irfan, M. Zhang, J. Li
College of Engineering Physics
Shenzhen Technology University
Shenzhen 518118, China
E-mail: lijia@sztu.edu.cn

The ORCID identification number(s) for the author(s) of this article can be found under https://doi.org/10.1002/pssr.202500110.

P. K. Chu
Department of Physics
Department of Materials Science and Engineering
Department of Biomedical Engineering
City University of Hong Kong
Tat Chee Avenue, Kowloon, Hong Kong, China

DOI: 10.1002/pssr.202500110

structure with distinct layers for more direct pathways and fewer recombination sites for charge carriers. It results in good mobility and efficient charge trapping effect (CTE) to benefit charge transport, response rate, power consumption, and device stability.[18,23,24] However, despite these merits, the performance of PHJ-based OPTs is still far from satisfactory and lags behind that of their BHJ counterparts. This partially stems from the difficulty in producing a high-quality organic interface with low defect density, large area, good uniformity, and low roughness, which are prerequisites to a superior planar interface and, in turn, optimal carrier dynamics of PHJ-OPTs.[25] Hence, in order to boost the photodetection efficiency of PHJ-OPTs upon NIR illumination, it is highly desirable to develop a high-quality PHJ with the appropriate D/A interactions, decent mobility, efficient NIR light absorption, and scalable processing.

Herein, a PHJ with the above merits is designed and demonstrated for high-performance NIR-OPTs. The PHJ is composed of a bilayer of a conjugated polymer, poly{2,2′-(2,5-bis(2-octyldodecyl)-3,6-dioxo-2,3,5,6-tetrahydropyrrolo[3,4-c]pyrrole-1,4-diyl) dithieno[3,2-b]thiophene-5,5′-diyl-alt-thiophen-2,5-diy (PDPPBTT) and a fullerene derivative, [6,6]-phenyl-C_{61}-butyric acid methyl ester ($PC_{61}BM$), with their molecular structures shown in **Figure 1**. The p-type polymeric semiconductor PDPPBTT plays the multifunctional roles of the conductive channel, electron donor, and NIR photoactive substance [26] while $PC_{61}BM$ acts as the electron acceptor. Instead of the traditional solution-based process, a simple and effective evaporation-assisted technique is developed to prepare the PHJ. Thermal evaporation is performed to directly deposit the $PC_{61}BM$ thin film on PDPPBTT to form the high-quality PDPPBTT/$PC_{61}BM$ PHJ. Evaporation produces $PC_{61}BM$ films with good uniformity, large area, small roughness, and controlled thickness control while avoiding the destruction of the PDPPBTT channel that occurs frequently in traditional solution processes (Figure S1, Supporting information). As a result, the high-quality PHJ with efficient CTE and fast transport pathway balances charge separation and transport. The NIR-OPTs deliver outstanding NIR photodetection performance in terms of sensitivity (2.59×10^4), responsivity (1.42×10^5 A W^{-1}), detectivity (1.83×10^{16} Jones), and detection limit of 70 nW cm^{-2} ($\lambda = 808$ nm).

2. Results and Discussion

The proof-of-concept device adopts a bottom-gate/top-contact structure fabricated in the SiO_2/n^+-Si substrate, as shown in Figure 1a. Atomic force microscopy (AFM) shows that the evaporated PHJ film has a uniform and smooth surface with a low root mean square roughness of 0.48 nm, as shown in Figure 1b. The absorption spectra of PDPPBTT and PDPPBTT/$PC_{61}BM$ PHJ are shown in Figure 1c. The PDPPBTT exhibits distinct light absorption in the NIR range, while light absorption in this wavelength range by $PC_{61}BM$ can be neglected, consequently corroborating the photoactive role of PDPPBTT. The working principle of the device is described in Figure 1d. During NIR illumination, electron-hole pairs (EHPs) are generated in the PDPPBTT photoactive layer. The energy offset between PDPPBTT and $PC_{61}BM$ dissociates the EHPs at the PDPPBTT/$PC_{61}BM$ planar heterointerface. Photo-induced electrons move from the lowest unoccupied molecular orbital (LUMO) of PDPPBTT to the LUMO of

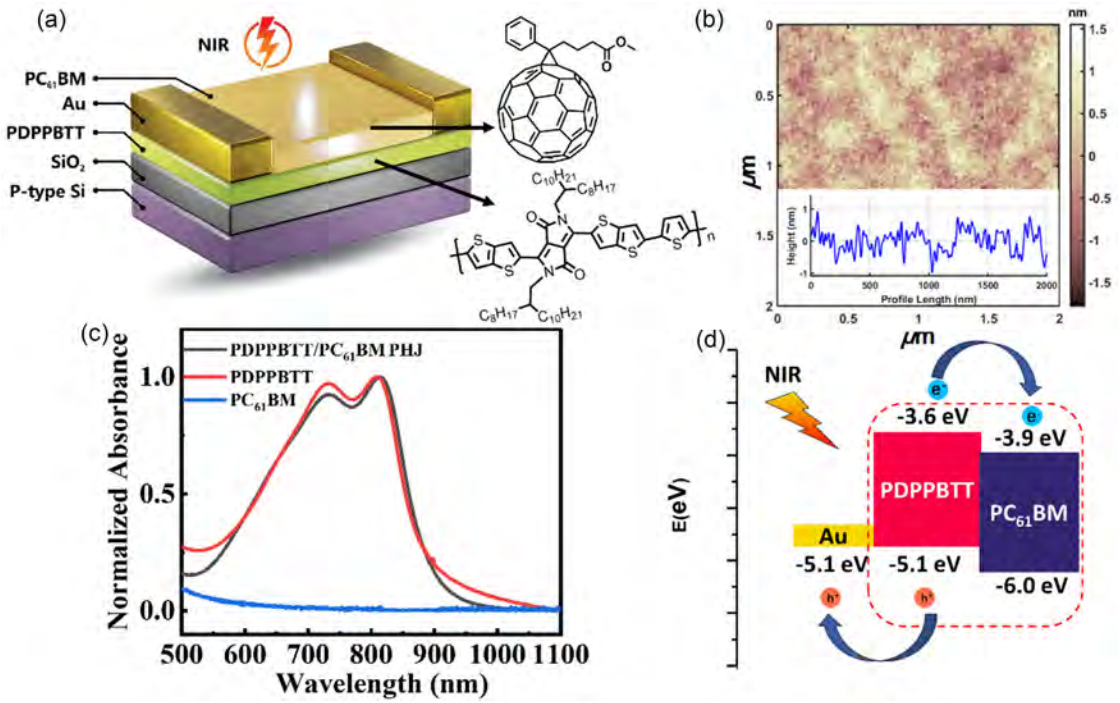

Figure 1. Device structure and photodetection mechanism: a) Schematic diagram of the device and the chemical structures of PDPPBTT and $PC_{61}BM$, b) AFM image of the PDPPBTT/$PC_{61}BM$ PHJ, c) Vis-NIR absorbance spectra of PDPPBTT, PDPPBTT/$PC_{61}BM$ PHJ, and $PC_{61}BM$, and d) Energy level diagram of the device upon illumination.

$PC_{61}BM$ and are trapped. On the other hand, the holes accumulate in the pure PDPPBTT channel layer. The steady-state photoluminescence (PL) spectra of the pure PDPPBTT and PDPPBTT/$PC_{61}BM$ PHJ thin films are shown in (Figure S2, Supporting Information). The PL intensity of the PDPPBTT/$PC_{61}BM$ PHJ thin film is less than that of the pure PDPPBTT, which implies that the charge transport or energy transfer occurs between the PDPPBTT and $PC_{61}BM$. When PDPPBTT and $PC_{61}BM$ molecules form a PHJ at the interface, the significant energy offset between their LUMO levels facilitates the separation of photo-generated EHPs in PDPPBTT. As a result, the photo-generated electrons can be efficiently captured by $PC_{61}BM$ molecules, leading to a lower PL intensity than that of pure PDPPBTT. The accumulated holes move in the channel layer under an electric field (i.e., V_D) to generate a photocurrent on account of the intrinsic gain effect. Consequently, the device combines the advantages of CTE and efficient carrier transport of the high-quality PDPPBTT/$PC_{61}BM$ PHJ.

The transfer characteristics of the field-effect transistors consisting of pure PDPPBTT, PDPPBTT/$PC_{61}BM$ BHJ, and PDPPBTT/$PC_{61}BM$ PHJ are presented in **Figure 2**a–c. The devices exhibit the typical transfer characteristics of p-type transistors with on/off rates of 10^3–10^5, indicating that the carrier densities of the PDPPBTT-based transistors can be adjusted by the gate voltage. The carrier mobilities of the pure PDPPBTT and PDPPBTT/$PC_{61}BM$ PHJ transistors are determined to be 0.35 and 0.37 $cm^{-2}\,V^{-1}\,s^{-1}$, respectively, implying that the evaporated $PC_{61}BM$ maintains the high-quality PDPPBTT channel and fast transport pathways in the NIR-OPTs. In contrast, the mobility of the BHJ-based transistors decreases significantly to 0.26 $cm^{-2}\,V^{-1}\,s^{-1}$ with the D/A concentration ratio of 5:1. The mobility decreases further with increasing D/A concentration ratios (Table S1, Supporting information) because the BHJ contains a large number of the D/A interfaces which trap more charges, increase the channel resistance, and decrease the carrier mobility. These effects give rise to more noise and recombination in conjunction with reduced gain and limited photodetectivity.

During exposure to NIR light ($\lambda = 808$ nm, 135 $\mu W\,cm^{-2}$), they exhibit a distinct photoresponse, characterized by an increase in the drain current I_D and a positive shift of the threshold voltage (V_{Th}), as shown in Figure 2a–c. These results suggest that the PDPPBTT photoactive layer generates free charged carriers. In addition, the heterostructure, i.e., either BHJ or PHJ, shows pronounced current enhancement and threshold voltage shift due to more efficient exciton dissociation. In particular, the comparison of their photosensitivities is shown in Figure 2d. One can see that the PHJ-OPT delivers superior photodetection performance manifested by higher photosensitivity (photocurrent/dark current) of 1.79×10^4, compared with BHJ-OPT (1.34×10^3) and pure PDPPBTT OPT (34.7). These results indicate that the PDPPBTT/$PC_{61}BM$ combination has efficient NIR light absorption and appropriate carrier dynamics, while not compromising the channel quality.[26,27]

The photoresponse of the PHJ-OPT for different irradiance powers and wavelengths is determined. **Figure 3**a shows the transfer characteristics of the PHJ-OPT for different irradiance powers with V_G scanned from 20 to −40 V and V_D fixed at −10 V. As a result of the enhanced irradiance power, the photocurrent increases steadily, and the threshold voltage shifts positively. The current increases because the hole concentration in the PDPPBTT channel increases during NIR illumination. The hole concentration can be estimated using the equation, $\Delta P = \frac{C_i \Delta V_{Th}}{e}$,

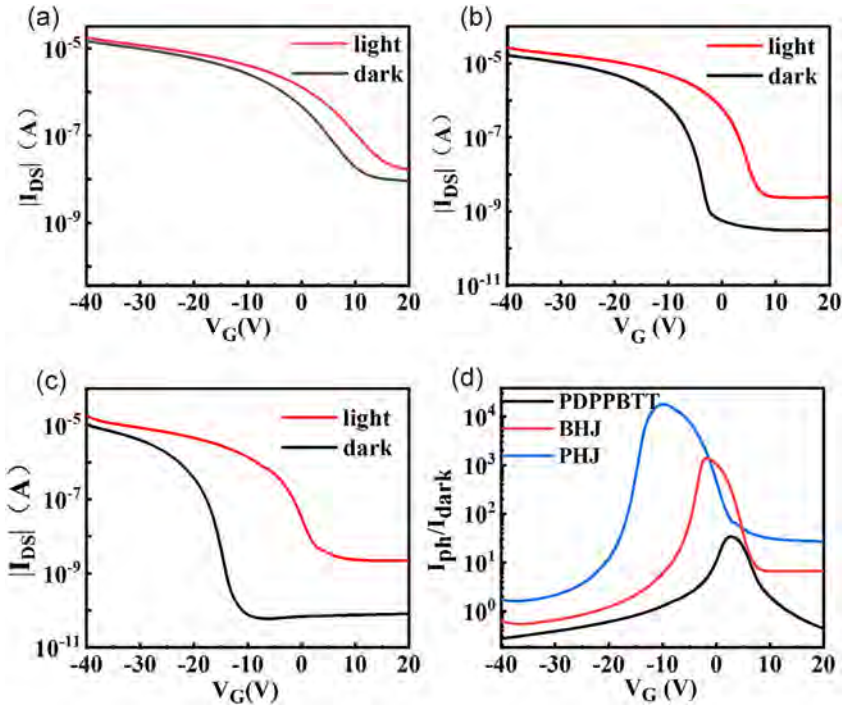

Figure 2. Light and dark transfer curves of a) Pure PDPPBTT phototransistor, b) PDPPBTT/$PC_{61}BM$ BHJ phototransistor, c) PDPPBTT/$PC_{61}BM$ PHJ phototransistor; d) photosensitivities of OPTs fabricated with pure PDPPBTT, PDPPBTT/$PC_{61}BM$ BHJ, and PDPPBTT/$PC_{61}BM$ PHJ.

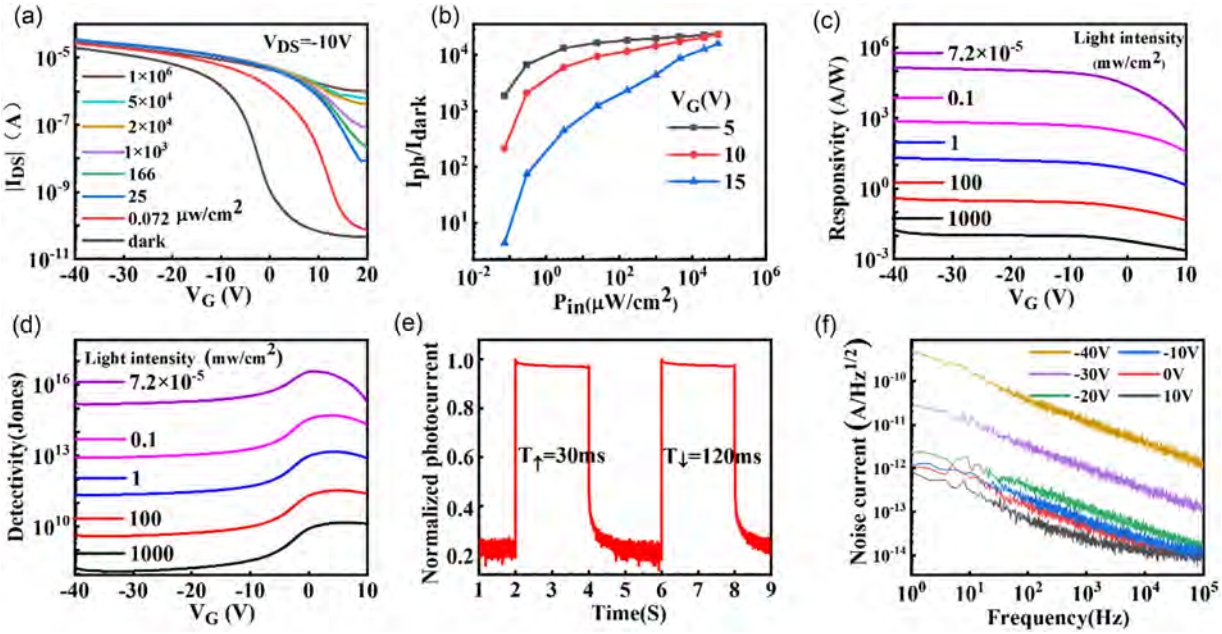

Figure 3. a) Transfer characteristics of the PHJ-OPT as a function of incident light intensity; b) Photosensitivity of the PHJ-OPT at different light intensities; c) Photoresponsivity of the PHJ-OPT under illumination of different light intensities; d) Detectivity of the PHJ-OPT for different light intensities. e) Rise and fall times of PHJ-OPT recorded under irradiation with a wavelength of 808 nm and a power density of 100 μW cm^{-2} ($V_G = 2$ V and $V_{DS} = -10$ V); f) Dark currents of PHJ-OPT for different gate voltages and frequencies.

where C_i is the unit area capacitance of the dielectric layer, ΔV_{Th} is the shift in the threshold voltage, and e is the elementary charge. During 32 mW cm^{-2} irradiation, the threshold voltage shift is 22.54 V, which corresponds to a larger hole concentration of 2.42×10^{12} cm^{-2}. The positive shift in the threshold voltage (ΔV_T) is caused by the photogating effect arising from the trapped photo-generated electrons and high-density holes in the conduction channel. The enhanced hole concentration in the PDPPBTT channel layer increases the photocurrent and also shifts the Fermi level toward the HOMO of PDPPBTT.[2,28,29] The photoinduced trapped electrons in $PC_{61}BM$ produce a negative gate bias V_G, which reduces the turn-on voltage of the OPT devices. It can be inferred that the high-quality channel and efficient CTE in the PHJ-OPT produce superior photoresponse. The conduction channel can be modulated by the gate voltage and turned off in the dark by operating the device in the depletion regime. The dark current of the PHJ-OPT is only about 30 pA, boding well for the detection of weak-light signals. In fact, the device is responsive to an ultralow irradiance power down to 0.072 μW cm^{-2}. (Figure S3, Supporting Information) shows the transfer characteristics of a PHJ-OPT during illumination by light of different wavelengths from 400 to 1,100 nm. The light intensity is fixed at 100 μW cm^{-2} and V_D at −10 V. Clearly, the trend is consistent with the Vis-NIR absorption spectra, confirming strong photoresponse to NIR light but weaker response in the visible region.

The photodetection efficiency of the PHJ-OPT is evaluated in terms of photosensitivity (I_{photo}/I_{dark}), photodetectivity, and photoresponsivity. Figure 3b shows the sensitivity as the function of irradiance power and gate voltage. The photosensitivity in the off-state with low dark currents is much higher than that in the on-state, and the maximum photosensitivity is observed near the threshold voltage (V_{th}) when the photo current and dark current have the largest variation. In addition, the photosensitivity increases with irradiance power, showing a maximum of 2×10^4 at 210 mW cm^{-2}. Notably, even for a very weak light (0.072 μW cm^{-2}), the photosensitivity still shows a peak of 10^3. Figure 3c presents the photoresponsivity of the PHJ-OPT as a function of V_G for different light intensities. The maximum R is 1.42×10^5 A W^{-1} for 0.072 μW cm^{-2} at $V_G = -40$ V. The specific detectivity (D^*) is another important Figure of merit for photodetectors. It indicates the photosensitivity and the noise limit of the photodetectors. Figure 3d shows the D^* values as a function of V_G for different light intensities at a fixed V_D of −10 V. D^* shows a similar trend with I_{photo}/I_{dark} reaching the peak at the turn-on gate voltage (i.e., −40 V). The peak of D^* of the PHJ-OPT is 1.86×10^{16} Jones. The time-dependent photoresponse of the heterojunction phototransistor (HJPT) is assessed by measuring the change in I_D during on-and-off light illumination. As shown in Figure 3e, the PHJ-OPT exhibits a reproducible photodetection behavior under alternating dark and light conditions. The rise and decay times of the HJPT device are 30 and 120 ms, respectively. Compared with other reported NIR-OPTs, our device delivers comparable and even better performance (Table S2, Supporting Information).

Reducing the dark current is crucial for OPTs as it is the main factor affecting the capability of detecting weaklight signals.[30,31] At a transverse bias of −40 and −5 V, the dark current of the device is only about 0.58 nA (Figure S4, Supporting Information), which is conducive to detecting extremely weak signals. Figure 3f shows the noise power spectrum of the device as the gate voltage changes from −40 to 10 V in the frequency range between 1 Hz

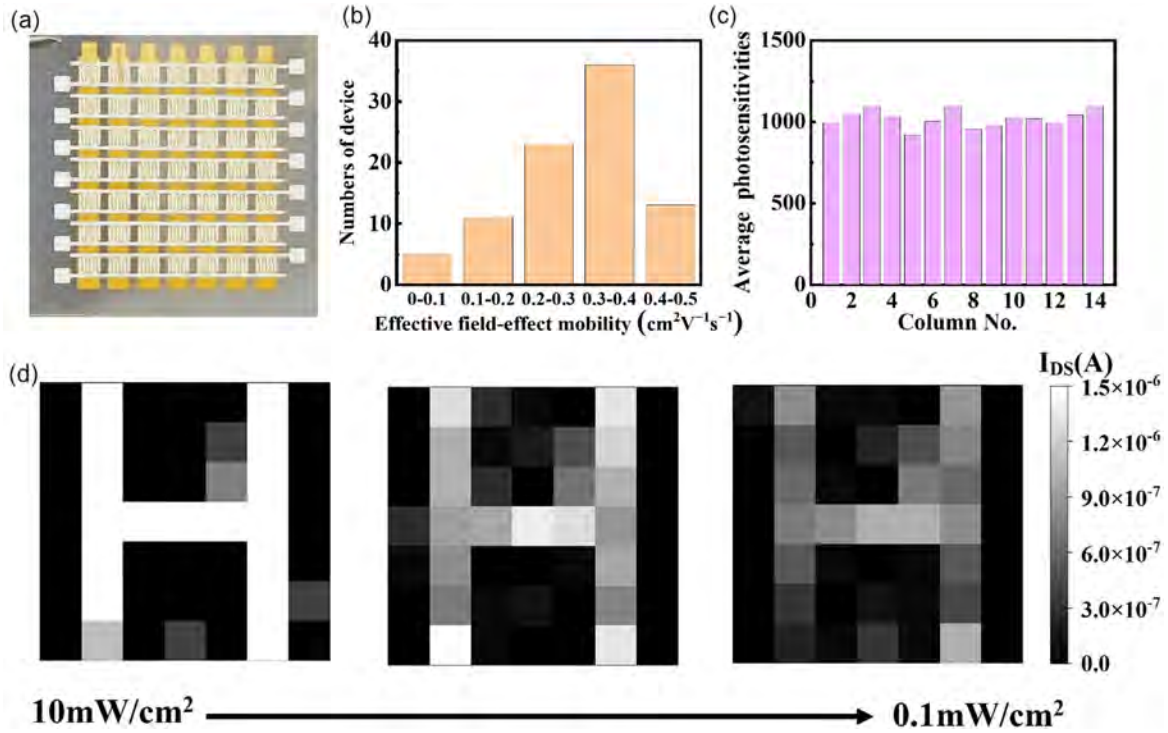

Figure 4. a) Image of the 7 × 7 array; b) Number of devices with different carrier mobilities; c) Average photosensitivities of the OPTs distributed in 14 columns; d) Image of the array for different optical power densities.

and 100 kHz. When the device is in the off state ($V_G = -10$ V), the noise current at low frequencies drops to 0.84 pA $Hz^{-1/2}$. The noise spectrum follows a $1/f$ relationship in the frequency range between 1 Hz and 100 kHz. Clearly, the conductive channel in the PHJ structure in the off state leads to a smaller dark current and smaller shot noise, the shot noise minimally affects the device's signal-to-noise ratio, enabling the device to maintain a high D^* under weak-light and low-frequency conditions, which lead the excellent capability to detect weak signals.

To evaluate the potential of imaging applications, OPTs based on the PDPPBTT/PC_{61}BM PHJ are prepared using a 7 × 7 pixel array, as shown in **Figure 4**a. In the array imaging system, the consistency of the overall device electrical properties and photosensitivity is crucial. The transfer characteristic curves of 98 single devices from two 7 × 7 array samples are acquired, and the carrier mobilities and photosensitivity for each single OPT are calculated. Figure 4b shows that the mobilities of most OPTs are between 0.1 and 0.5 $cm^{-2}v^{-1}s^{-1}$, boding well for OPTs-based imaging.[32] To further assess the overall uniformity of the array, we have also calculated the V_{Th} and transconductance. We obtained an average transconductance of 6.8×10^{-6} S with a standard deviation of 0.6×10^{-6} S, and an average V_{Th} of −2.4 V with standard deviation of 0.13 V. These results indicate that our array has good uniformity for future array-based applications. Figure 4c shows the average photosensitivities of OPTs distributed in 14 columns, and they are relatively high and evenly distributed. A metallic shadow mask with an "*H*" pattern is placed between the NIR light source and the imager, and images are captured by illuminating the shadow masks with NIR light. Most of the image pixels work properly, and the "*H*" pattern can be clearly identified. The image quality is evaluated for different NIR irradiances, which decrease gradually from 10 to 0.1 mW cm^{-2}. The brightness depends on the irradiance, suggesting a good dynamic response to light illumination.

3. Conclusion

In summary, a proof-of-concept device based on the PDPPBTT/PC_{61}BM PHJ is designed and demonstrated for organic NIR phototransistors. The device combines the merits of good mobility, high NIR absorption, and efficient CTE to achieve high-gain and ultrasensitive NIR photodetection. The fabricated PHJ-OPTs deliver outstanding performance, such as high photosensitivity of 2.59×10^4, photoresponsivity of 1.42×10^5 A W^{-1}, and photodetectivity of 1.86×10^{16} Jones in spite of weaklight exposure. The fully integrated planar device architecture boasts a good balance between sensitive NIR detection, low cost, and easy fabrication. Overall, the efficient PDPPBTT/PC_{61}BM PHJ opens up new opportunities for both fundamental research and high-performance NIR photodetection.

4. Experimental Section

Materials: PDPPBTT and PC_{61}BM were purchased from Luminescence Technology Corp. (Lumtec) and used without further purification, and OTS ($C_{18}H_{37}Cl_3Si$) was purchased from Shanghai Aladdin Biochemical Technology Co., Ltd. (Aladdin). The PDPPBTT solution was prepared by dissolving PDPPBTT in chloroform and stirring for 12 h at 60 °C. All the solutions were filtered through an Acrodisc PTFE syringe filter (Millipore 0.22 μm) prior to spin coating.

Device Fabrication: The phototransistors with the bottom-gate/top-contact configuration were fabricated on silicon wafers (Si/SiO_2). The Si/SiO_2 substrates were sequentially ultrasonicated in acetone, isopropanol, and deionized water for 10 min each, and then treated with UV/ozone for 15 min. Subsequently, the substrates were immersed in an OTS solution with a volume ratio of 1:500 at 60 °C for 15 min in a glove box. The substrates were then taken out and sequentially ultrasonicated in toluene, acetone, absolute ethanol, and deionized water for 10 min each. A 30 nm thick PDPPBTT film was deposited on the OTS film by either spin coating or self-assembly. With regard to the spin-coated devices, the PDPPBTT solution was spin-coated on the OTS film at 2,000 rpm for 60 s and then annealed at 150 °C for 30 min. Afterward, the Au source and drain electrodes (30 nm) were evaporated thermally through a shadow mask. The channel length (L) and width (W) of the devices were 70 and 1,050 μm, respectively. Finally, a 10 nm thick $PC_{61}BM$ film was deposited on the PDPPBTT film by thermal evaporation.

In the preparation of the 7×7 array devices, after cleaning the substrate by the aforementioned cleaning process, a 50 nm thick gold film was deposited to form the gate electrode by shadow masking. A 30 nm thick Al_2O_3 film was deposited as the insulating layer by atomic layer deposition (ALD). After modifying the surface of the Al_2O_3 with OTS (octadecyl trichlorosilane) to improve the interface, PDPPBTT, Ag, and $PC_{61}BM$ were sequentially deposited as described above.

Characterization and Calculation: Electrical characterization (I–V, noise, response bandwidth) was carried out on the phototransistors under ambient conditions on the FS-Pro semiconductor parameter analyzer equipped with a standard probe station. During light detection, the device and light source were placed in a metal box to avoid influence by ambient light. The light intensity was calibrated by a THORLABS PM100D optical power meter. The photoresponse spectra of the phototransistors were acquired using an SC-PRO supercontinuum source and an 808 nm laser. The PL spectra were recorded by using a fluorescence spectrophotometer (FLS1000, Edinburgh) with an 808 nm laser as the excitation source.

The carrier mobility of the device was calculated by the following equation.

$$\mu_{FE} = \frac{2L}{WC_i}\left(\frac{\partial\sqrt{I_{SD}}}{\partial V_G}\right)^2$$

where L is the channel length, W is the channel width, C_i is the capacitance per unit area of the gate dielectric, I_{SD} is the source–drain current, and V_G is the gate voltage. The specific detectivity was calculated by the following equation.

$$D^* = \frac{R\sqrt{A}}{\sqrt{2qI_{dark}}}$$

where R is the optical responsivity and an important parameter, which was derived by the following equation.

$$R = \frac{I_{ph}}{P_{in}} = \frac{I_{light} - I_{dark}}{P_{in}}$$

where I_{ph} is the photocurrent, P_{in} is the optical power incident on the channel, A is the device conductive channel area, q is the elementary charge of the electron, and I_{dark} is the dark current.

Supporting Information

Supporting Information is available from the Wiley Online Library or from the author.

Acknowledgements

The authors acknowledge the support from the National Natural Science Foundation of China (12474433&11974371), Key Area Funds of Universities of Guangdong Province (2023ZDZX1021), Research Talent Start-Up Fund of SZTU(GDRC202140 & GDRC202201), Shenzhen Science and Technology Research Funding (JCYJ20220818101412027 & JCYJ20241202124900002), and City University of Hong Kong Donation Research Grants (9220061 and DON-RMG 9229021).

Conflict of Interest

The authors declare no conflict of interest.

Author Contributions

Liye Yang: conceptualization (lead); data curation (lead); formal analysis (equal); investigation (equal); software (equal). **Shuai Sun**: data curation (equal). **Liangyu Zhang**: data curation (equal). **Muhammad Irfan**: data curation (equal). **Mengpei Zhang**: data curation (equal). **Paul K. Chu**: data curation (equal). **Yang Jiao**: data curation (equal). **Jia Li**: conceptualization (lead); data curation (equal); formal analysis (equal); funding acquisition (lead); investigation (equal); methodology (lead); project administration (lead); resources (lead); software (equal); supervision (lead); validation (equal); visualization (equal); writing—original draft (supporting); writing—review & editing (lead).

Data Availability Statement

The data that support the findings of this study are available in the supplementary material of this article.

Keywords

near-infrared detectors, near-infrared imaging, organic photodetectors, organic phototransistors, planar heterojunctions

Received: March 12, 2025
Revised: May 10, 2025
Published online: June 20, 2025

[1] C. Wang, X. T. Zhang, W. P. Hu, *Chem. Soc. Rev.* **2020**, *49*, 653.
[2] K. Welsher, Z. Liu, D. Daranciang, H. Dai, *Nano Lett.* **2008**, *8*, 586.
[3] Z. Y. He, J. Y. Han, X. Y. Du, L. Y. Cao, J. Wang, C. J. Zheng, H. Lin, S. L. Tao, *Adv. Funct. Mater.* **2021**, *31*, 2103988.
[4] Y. S. Rim, Y. Yang, S. H. Bae, H. J. Chen, C. Li, M. S. Goorsky, Y. Yang, *Adv. Mater.* **2015**, *27*, 6885.
[5] H. T. Li, J. L. Liu, Y. K. Dong, C. Fei, Y. F. Li, S. L. Yang, S. Z. Fan, Y. X. Liu, X. Zhao, *Meas. Sci. Technol.* **2025**, *36*, 035202.
[6] C. Y. Tang, C. Y. Lu, Q. Y. Dai, N. B. Zhang, L. Sun, S. N. Xu, Y. Q. Peng, W. L. Lv, *Semicond. Sci. Technol.* **2022**, *37*, 075014.
[7] J. Kublitski, A. Fischer, S. Xing, L. Baisinger, E. Bittrich, D. Spoltore, J. Benduhn, K. Vandewal, K. Leo, *Nat. Commun.* **2021**, *12*, 4259.
[8] H. Q. Shan, Y. L. Wang, C. Li, Q. K. Hu, X. Z. Sun, L. Dong, Y. M. Feng, W. K. Ye, J. J. Xu, Z. X. Xu, *Org. Electron.* **2018**, *58*, 197.
[9] Q. Y. Dai, G. Hu, W. L. Lv, S. A. Xu, L. Sun, G. F. Schneider, L. Jiang, Y. Q. Peng, *Adv. Mater. Interfaces* **2022**, *9*, 2200116.
[10] C. O. Quero, I. Rondon, J. Martinez-carranza, *J. Opt. Soc. Am. A* **2025**, *42*, 201.
[11] M. H. Shou, Q. L. Zhang, Y. Zhang, X. H. Hou, J. X. Zheng, J. D. Zhou, S. C. Xiong, N. Zheng, Z. Q. Xie, L. L. Liu, *J. Mater. Chem. C* **2022**, *10*, 16070.
[12] W. Wang, Y. J. Deng, S. Sun, M. Galluzzi, Y. Jiao, P. K. Chu, Z. R. Li, J. Li, J. Q. Yao, *Adv. Electron. Mater.* **2024**, *10*, 2400128.

[13] H. H. Xu, J. Liu, J. Zhang, G. D. Zhou, N. Q. Luo, N. Zhao, *Adv. Mater.* **2017**, *29*, 1700975.
[14] R. Shyam, P. K. Aich, U. Pandey, B. N. Pal, R. Prakash, *IEEE Sens. J.* **2024**, *24*, 32004.
[15] M. A. Rahman, H. Kim, Y. K. Lee, C. Lee, H. Nam, J. S. Lee, H. Soh, J. K. Lee, E. G. Lee, J. Lee, *J. Nanosci. Nanotechnol.* **2012**, *12*, 1348.
[16] C. R. Liu, S. C. Xiong, D. Sun, Z. Q. Xie, L. L. Liu, *J. Mater. Chem. C* **2024**, *12*, 16100.
[17] Y. H. Gao, Y. Yi, X. W. Wang, H. Meng, D. Y. Lei, X. F. Yu, P. K. Chu, J. Li, *Adv. Mater.* **2019**, *31*, 1900763.
[18] H. Y. Yu, X. L. Zhao, M. Y. Tan, B. Wang, M. X. Zhang, X. Wang, S. L. Guo, Y. H. Tong, Q. X. Tang, Y. C. Liu, *Adv. Funct. Mater.* **2022**, *32*, 2206765.
[19] Z. Xu, *J. Soc. Inf. Disp.* **2000**, *8*, 0734.
[20] Y. Zhang, Y. C. Qiu, X. Y. Li, Y. W. Guo, S. Q. Cao, H. F. Gao, Y. C. Wu, L. Jiang, *Small* **2022**, *18*, 2203429.
[21] X. Sha, Y. Cao, L. Q. Meng, Z. Q. Yao, Y. H. Gao, N. Zhou, Y. Zhang, P. L. K. Chu, J. Li, *Appl. Phys. Lett.* **2022**, *120*, 151103.
[22] Y. Q. Peng, W. L. Lv, B. Yao, G. Y. Fan, D. Q. Chen, P. J. Gao, M. Q. Zhou, Y. Wang, *Org. Electron.* **2013**, *14*, 1045.
[23] Y. J. Yin, Z. Y. Xi, Q. Yu, X. Y. Gong, H. A. Wang, B. Yao, H. T. Xu, J. Shi, L. Y. Yin, W. J. Yang, X. Zhang, Y. X. Wei, X. Luo, Z. B. Fang, *Results Phys.* **2023**, *48*, 106456.
[24] B. Yang, Y. Wang, L. Li, J. Y. Zhang, J. L. Wang, H. X. Jiao, D. D. Hao, P. Guo, S. Zeng, Z. K. Hua, J. Huang, *Adv. Funct. Mater.* **2021**, *31*, 2103787.
[25] Y. L. Liang, W. L. Lv, X. Luo, L. He, K. Xu, F. Y. Zhao, F. B. Huang, F. P. Lu, Y. Q. Peng, *Synth. Met.* **2018**, *240*, 44.
[26] M. H. Shou, Q. L. Zhang, S. C. Xiong, T. Han, J. D. Zhou, N. Zheng, Z. Q. Xie, L. L. Liu, *ACS Appl. Mater. Interfaces* **2021**, *13*, 5293.
[27] F. Pan, X. R. Qian, L. Z. Huang, H. B. Wang, D. H. Yan, *Chin. Phys. Lett.* **2011**, *28*, 078504.
[28] B. R. Sutherland, A. K. Johnston, A. H. Ip, J. X. Xu, V. Adinolfi, P. Kanjanaboos, E. H. Sargent, *ACS Photonics* **2015**, *2*, 1117.
[29] Y. Wang, Q. F. Liao, D. H. She, Z. Y. Lv, Y. Gong, G. L. Ding, W. B. Ye, J. R. Chen, Z. Y. Xiong, G. P. Wang, Y. Zhou, S. T. Han, *ACS Appl. Mater. Interfaces* **2020**, *12*, 15370.
[30] Z. J. Zhao, C. Y. Xu, L. B. Niu, X. L. Zhang, F. J. Zhang, *Laser Photonics Rev.* **2020**, *14*, 2000262.
[31] Y. H. Gao, S. Sun, D. Qiu, Y. M. Wei, M. P. Zhang, J. Liu, P. K. Chu, W. L. You, J. Li, *ACS Photonics* **2023**, *10*, 764.
[32] D. W. Li, Z. R. Jia, Y. J. Tang, C. Y. Song, K. Liang, H. H. Ren, F. F. Li, Y. T. Chen, Y. Wang, X. Y. Lu, L. Meng, B. W. Zhu, *Nano Lett.* **2022**, *22*, 5434.